

Band nesting, massive Dirac fermions, and valley Landé and Zeeman effects in transition metal dichalcogenides: A tight-binding model

Maciej Bieniek,^{1,2} Marek Korkusiński,^{1,3} Ludmiła Szulakowska,¹ Paweł Potasz,^{1,2} Isil Ozfidan,⁴ and Paweł Hawrylak¹

¹Department of Physics, University of Ottawa, Ottawa, Ontario, Canada K1N 6N5

²Department of Theoretical Physics, Wrocław University of Science and Technology, Wybrzeże Wyspiańskiego 27, 50-370 Wrocław, Poland

³Security and Disruptive Technologies, Emerging Technologies Division, NRC, Ottawa, Canada K1A 0R6

⁴D-Wave Systems, Vancouver, British Columbia, Canada V7X 1L3



(Received 9 May 2017; revised manuscript received 26 January 2018; published 27 February 2018)

We present here the minimal tight-binding model for a single layer of transition metal dichalcogenides (TMDCs) MX_2 (M , metal; X , chalcogen) which illuminates the physics and captures band nesting, massive Dirac fermions, and valley Landé and Zeeman magnetic field effects. TMDCs share the hexagonal lattice with graphene but their electronic bands require much more complex atomic orbitals. Using symmetry arguments, a minimal basis consisting of three metal d orbitals and three chalcogen dimer p orbitals is constructed. The tunneling matrix elements between nearest-neighbor metal and chalcogen orbitals are explicitly derived at K , $-K$, and Γ points of the Brillouin zone. The nearest-neighbor tunneling matrix elements connect specific metal and sulfur orbitals yielding an effective 6×6 Hamiltonian giving correct composition of metal and chalcogen orbitals but not the direct gap at K points. The direct gap at K , correct masses, and conduction band minima at Q points responsible for band nesting are obtained by inclusion of next-neighbor Mo-Mo tunneling. The parameters of the next-nearest-neighbor model are successfully fitted to MX_2 ($M = \text{Mo}$; $X = \text{S}$) density functional *ab initio* calculations of the highest valence and lowest conduction band dispersion along K - Γ line in the Brillouin zone. The effective two-band massive Dirac Hamiltonian for MoS_2 , Landé g factors, and valley Zeeman splitting are obtained.

DOI: [10.1103/PhysRevB.97.085153](https://doi.org/10.1103/PhysRevB.97.085153)

I. INTRODUCTION

There is currently renewed interest in understanding the electronic and optical properties of transition metal dichalcogenides (TMDCs) with formula MX_2 (M , metal from group IV to VI; $X = \text{S}, \text{Se}, \text{Te}$) [1–31]. Recent experiments and *ab initio* calculations show that while bulk TMDCs are indirect gap semiconductors, single layers are direct gap semiconductors with direct gaps at K points of the Brillouin zone [1–31]. The existence of the gaps at K points of the Brillouin zone (BZ) could be anticipated from graphene, as the two materials share the hexagonal lattice. If in graphene we were to replace one sublattice with metal atoms and a second with chalcogen dimers, we might expect band structure similar to graphene but with opening of a gap at K points in the BZ. If this analogy was correct, the gap opening in a spectrum of Dirac fermions would lead to massive Dirac fermions and nontrivial topological properties associated with broken inversion symmetry and valley degeneracy. However, in graphene the band structure can be understood in terms of a tight-binding model with electrons tunneling between nearest-neighbor's p_z orbitals. The tunneling between next nearest neighbors, i.e., atoms on the same sublattice, modifies only slightly the electron and hole dispersion. The results of *ab initio* calculations [2–4,7,8,18,21,22,24] for MX_2 show that the conduction band (CB) minima and valence band (VB) maxima wave functions are composed primarily of metal d orbitals, i.e., next nearest neighbors. If only metal orbitals are retained the lattice structure changes from hexagonal to

triangular and the physics changes. Additional complication is the presence of secondary conduction band minima at Q points, at intermediate wave vectors between K and Γ points. These minima lead to conduction and valence band nesting which significantly enhances interactions of TMDCs with light [7,18,29]. A tight-binding model which illuminates these aspects and allows for inclusion of magnetic field, confinement, and many-body interactions is desirable.

There are already many tight-binding approaches to TMDCs by, e.g., Rostami *et al.* [32], Liu *et al.* [33], Cappelluti *et al.* [34], Zahid *et al.* [35], Fang *et al.* [36], and others [37–43], as well as $k \cdot p$ approaches [44–47]. These approaches are driven by the goal to reproduce in the best possible way the results of *ab initio* calculations. For example, Cappelluti *et al.* [34] provide a very detailed analysis of the tight-binding Hamiltonian in the basis of 3 Mo d orbitals and 3 p sulfur dimer orbitals, including analysis at high symmetry points. Fang *et al.* [36] derive a tight-binding Hamiltonian by transforming the *ab initio* Kohn-Sham Hamiltonian in plane wave basis into localized basis of Wannier orbitals. Each of the many contributions brings new physics and adds to our understanding of TMDCs. Our work aims at providing a physical, intuitive, understanding of the electronic states in a single layer of TMDC. We focus on the role of different d orbitals of the Mo atom and p orbitals of its three nearest-neighbor sulfur dimers and of hexagonal lattice. We derive an analytical expression for the tunneling matrix element analogous to the matrix element describing tunneling between two sublattices of graphene derived by Wallace [48]. We derive the selection

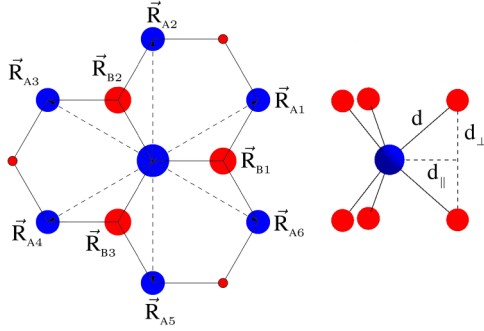


FIG. 1. Structure of MX_2 : blue Mo atoms; red sulfur atoms. Vectors $\vec{R}_{B1}, \vec{R}_{B2}, \vec{R}_{B3}$ point to nearest neighbors of central Mo atom and $\vec{R}_{A1} - \vec{R}_{A6}$ to next nearest neighbors of Mo atom.

rules coupling d and p orbitals and show that they change between two nonequivalent K points and the Γ point. This demonstrates that the d orbitals must cross between Γ and K points resulting in a minimum in the conduction band at the Q point. We show that neither nearest-neighbor nor the three band model is capable of reproducing previous theoretical works as well as our *ab initio* results [7,24]. With the understanding of the subtleties of the electronic band structure we generate the simplest tight-binding model which illuminates the physics of TMDCs, especially the role of hexagonal lattice, tunneling from metal to dimer orbitals, band nesting, and enhanced joint optical density of states. The model reduces to the effective two band massive Dirac fermion model yielding Landé g factors, valley Zeeman splitting, and Landau levels.

II. MODEL

We start with the structure of a single layer of MX_2 and for definiteness we focus on MoS_2 . Figure 1 shows the top view of a fragment of MoS_2 hexagonal lattice, with Mo positions marked with blue circles and sulfur dimers marked with red circles. The lattice structure is almost identical to graphene; the differences are visible in the side view showing the sulfur dimers and three, sulfur-metal-sulfur, layers of a single layer of MoS_2 . Figure 1 shows a central metal atom (large blue circle) of sublattice A surrounded by three first neighbor sulfur dimers of sublattice B marked with positions \vec{R}_{B1} , \vec{R}_{B2} , and \vec{R}_{B3} . The positions of second neighbors belonging to metal sublattice A are marked with $\vec{R}_{A1}, \dots, \vec{R}_{A6}$. We now construct the wave function out of orbitals localized on metal atoms and sulfur dimers. We start by selecting orbitals on a metal atom. Guided by results of *ab initio* calculations [7] we first consider d orbitals $l = 2$, with $m_d = \pm 2, \pm 1, 0$. Out of five m_d orbitals, orbitals with $m_d = \pm 2, 0$ are even with respect to the Mo layer. We select three d orbitals $\varphi_{l=2, m_d}(\vec{r} - \vec{R}_{A,i})$ localized on i th Mo atom of sublattice A at $\vec{R}_{A,i}$. For a sulfur dimer we select three p orbitals with $l = 1, m_p = \pm 1, 0$ on lower (L) and upper (U) sulfur atoms. We first construct dimer orbitals which are even with respect to the Mo plane:

$$\varphi_{l=1, m_p=\pm 1}(\vec{r}) = \frac{1}{\sqrt{2}} [\varphi_{l=1, m_p=\pm 1}^U(\vec{r}) + \varphi_{l=1, m_p=\pm 1}^L(\vec{r})]$$

and

$$\varphi_{l=1, m_p=0}(\vec{r}) = \frac{1}{\sqrt{2}} [\varphi_{l=1, m_p=0}^U(\vec{r}) - \varphi_{l=1, m_p=0}^L(\vec{r})].$$

We note the minus sign in the $m_p = 0$ orbital due to odd character of $m = 0$ p_z orbital. With three orbitals on Mo atom we can write the wave functions on the sublattice A for each wave vector \vec{k} and orbital m_d as

$$\Psi_{A, m_d}^{\vec{k}}(\vec{r}) = \frac{1}{\sqrt{N_{UC}}} \sum_{i=1}^{N_{UC}} e^{i\vec{k} \cdot \vec{R}_{A,i}} \varphi_{l=2, m_d}(\vec{r} - \vec{R}_{A,i}), \quad (1)$$

where N_{UC} is the number of unit cells. In the same way we can write the three wave functions for sublattice B of sulfur dimers:

$$\Psi_{B, m_p}^{\vec{k}}(\vec{r}) = \frac{1}{\sqrt{N_{UC}}} \sum_{i=1}^{N_{UC}} e^{i\vec{k} \cdot \vec{R}_{B,i}} \varphi_{l=1, m_p}(\vec{r} - \vec{R}_{B,i}). \quad (2)$$

We now seek the LCAO electron wave function $\Psi_n^{\vec{k}}(\vec{r}) = [\sum_{m_d} A_{m_d}^{\vec{k}}(n) \Psi_{A, m_d}^{\vec{k}}(\vec{r}) + \sum_{m_p} B_{m_p}^{\vec{k}}(n) \Psi_{B, m_p}^{\vec{k}}(\vec{r})]$ with coefficients $A_{m_d}^{\vec{k}}(n)$, $B_{m_p}^{\vec{k}}(n)$ for band “ n ” and wave vector \vec{k} to be obtained by diagonalizing the Hamiltonian matrix in the space of wave functions $\Psi_{A, m_d}^{\vec{k}}(\vec{r})$ and $\Psi_{B, m_p}^{\vec{k}}(\vec{r})$.

III. NEAREST-NEIGHBOR TUNNELING HAMILTONIAN

We now proceed to construct matrix elements $\langle \Psi_{A, m_d}^{\vec{k}} | \hat{H} | \Psi_{B, m_p}^{\vec{k}} \rangle$ of the Hamiltonian describing tunneling from Mo orbitals to sulfur dimer orbitals. The matrix elements for tunneling from Mo atom in Fig. 1 to its three nearest neighbors \vec{R}_{B1} , \vec{R}_{B2} , and \vec{R}_{B3} can be explicitly written in analogy to graphene:

$$\begin{aligned} & \langle \Psi_{A, m_d}^{\vec{k}} | \hat{H} | \Psi_{B, m_p}^{\vec{k}} \rangle \\ &= \int d\vec{r} \varphi_{l=2, m_d}^*(\vec{r}) V_A(\vec{r}) [e^{i\vec{k} \cdot \vec{R}_{B1}} \varphi_{l=1, m_p}(\vec{r} - \vec{R}_{B1}) \\ &+ e^{i\vec{k} \cdot \vec{R}_{B2}} \varphi_{l=1, m_p}(\vec{r} - \vec{R}_{B2}) + e^{i\vec{k} \cdot \vec{R}_{B3}} \varphi_{l=1, m_p}(\vec{r} - \vec{R}_{B3})], \end{aligned} \quad (3)$$

where $V_A(r)$ is a potential on sublattice A. We can evaluate matrix elements, Eq. (3), at the K point of the Brillouin zone ($K = [0, 4\pi/(3\sqrt{3}d_{||})]$) to obtain

$$\begin{aligned} & \langle \Psi_{A, m_d}^{\vec{k}=K} | \hat{H} | \Psi_{B, m_p}^{\vec{k}=K} \rangle \\ &= (1 + e^{i(1-m_d+m_p)2\pi/3} + e^{i(1-m_d+m_p)4\pi/3}) V_{pd}(m_d, m_p), \end{aligned} \quad (4)$$

where $V_{pd}(m_d, m_p)$ is a Slater-Koster matrix element for tunneling from Mo atom orbital m_d to nearest sulfur dimer orbital m_p . We see in Eq. (4) that tunneling from central Mo atom to three nearest-neighbor sulfur dimers generates additional phase factors which depend on the angular momentum of orbitals involved. These additional phase factors are zero for carbon p_z orbitals in graphene and the quantum interference in tunneling amplitude, Eq. (4), vanishes and gap closes. In TMDCs the tunneling amplitude, Eq. (4), must lead to the removal of the degeneracy of d orbitals and hence must be finite.

The pairs of orbitals giving a nonvanishing tunneling matrix element must satisfy selection rule $1 + m_p - m_d = 0, \pm 3$. The only pairs of orbitals which satisfy this rule at K point are

$$[m_d = 0, m_p = -1], [m_d = 2, m_p = 1], [m_d = -2, m_p = 0]. \quad (5)$$

Hence the Hamiltonian at the K point is block-diagonal. Similar calculations lead to different selection rules at the nonequivalent $-K$ point:

$$[m_d = 0, m_p = 1], [m_d = -2, m_p = -1], [m_d = 2, m_p = 0], \quad (6)$$

while at the Γ point different pairs of orbital are coupled:

$$[m_d = 0, m_p = 0], [m_d = 2, m_p = -1], [m_d = -2, m_p = 1]. \quad (7)$$

$$H(\vec{k}) = \begin{pmatrix} E_{m_d=-2} & 0 & 0 & V_1 f_{-1}(\vec{k}) & -V_2 f_0(\vec{k}) & V_3 f_1(\vec{k}) \\ & E_{m_d=0} & 0 & -V_4 f_0(\vec{k}) & -V_5 f_1(\vec{k}) & -V_4 f_{-1}(\vec{k}) \\ & & E_{m_d=2} & -V_3 f_1(\vec{k}) & -V_2 f_{-1}(\vec{k}) & V_1 f_0(\vec{k}) \\ E_{m_p=-1} & 0 & 0 & & & \\ & E_{m_p=0} & 0 & & & \\ & & E_{m_p=1} & & & \end{pmatrix}. \quad (8)$$

We parametrize tunneling matrix elements, $H_{ij} = t_{ij}$, of Eq. (8) with tunneling parameter t . $t = 0$ means no tunneling and $t = 1$ means full tunneling matrix, Eq. (8). Figure 2 shows the evolution of the energy spectrum of the first-nearest-neighbor Hamiltonian at K point, Eq. (8), as a function of tunneling strength t . At $t = 0$ we have three degenerate d orbitals with energies E_d and three degenerate p orbitals on sulfur dimers with energy E_p . As the tunneling from Mo to S_2 orbitals is turned on the degeneracy of d orbitals is removed as they start hybridizing with p orbitals. The orbital $m_d = 2$ is the lowest energy valence band orbital. The $m_d = 0$ evolves

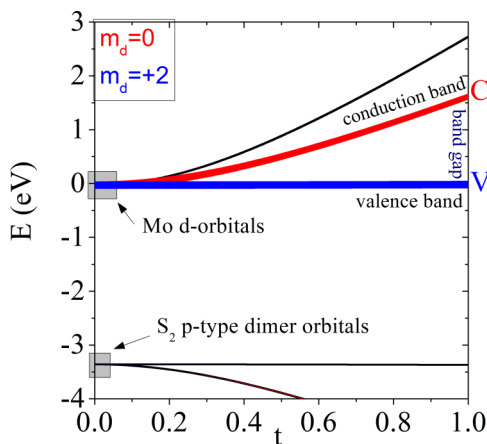


FIG. 2. Evolution of eigenenergies at K point as a function of tunneling matrix element t between Mo d and S_2 dimer p orbitals. Orbital composition: red circles $m_d = 0$; blue circles $m_d = +2$. Conduction band C and valence band V are marked. Lower energy orbitals are S_2 p orbitals. The removal of degeneracy of d orbitals and opening of the gap between $m_d = 0$ and $m_d = +2$ orbitals is shown. All energies are measured from the top of the valence band V .

We see that the three m_d orbitals are coupled to a different p dimer orbital each. Which pairs are coupled depends on the K and Γ points. This has important consequences for the response to magnetic field discussed later. We can now write the tunneling Hamiltonian with first-nearest-neighbor tunneling only. Here we put together the group of three degenerate d orbitals of S_2 . The tunneling matrix elements depend on tunneling amplitudes V_i with dependence on \vec{k} expressed by functions $f_i(\vec{k})$. The function $f_0(\vec{k})$ is the only function finite at $K = [0, 4\pi/(3\sqrt{3}d_{||})]$. Looking at the tunneling matrix elements of Hamiltonian, Eq. (8), containing $f_0(\vec{k})$ gives the coupled pairs of orbitals given by Eq. (5). Explicit forms of $f_i(\vec{k})$ and V_i are given in Appendix A:

as a conduction band orbital and $m_d = -2$ gives rise to the higher energy conduction band orbital. The magnitude of the band gap is fitted to the *ab initio* result using ABINIT and ADF [7,24].

Figure 3 shows the energy bands across the BZ obtained by fitting the first neighbor Hamiltonian, Eq. (8), using genetic algorithm to *ab initio* results obtained using ABINIT [7,24]. We see that such a simple Hamiltonian predicts a correct, finite, gap at K point but it also predicts closing of the gap in the Brillouin zone, here shown between M and Γ points. The closing of the gap is a consequence of the reversal of the role of $m_d = 0$ d orbital: it is a conduction band orbital

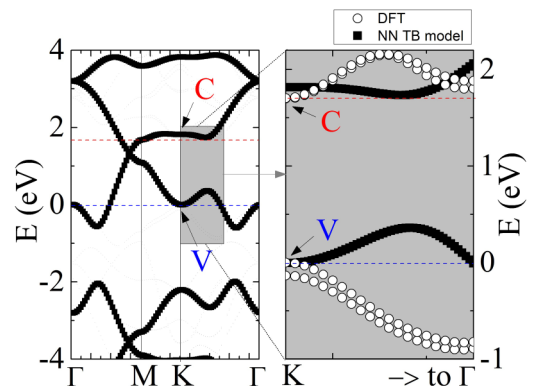


FIG. 3. Nearest-neighbor tunneling model. Black, TB model; white circles, DFT (no SO). Left: energy bands from K to Γ , K to M , and M to Γ points in the Brillouin zone obtained for MoS_2 with only nearest-neighbor tunneling included. Note band gap closing along M - Γ direction due to different symmetry of Mo orbitals at K and Γ . Right: comparison of C and V bands close to K point. Note local energy gap at K point but incorrect masses leading to lowest energy gap between K and Γ points.

at K point but valence band orbital at Γ . Therefore, without level repulsion there must be closing of the gap. In the right panel we also show a closeup of the dispersion of valence and conduction band along the K - Γ line. We see that the gap at K point is correct but the masses of holes and electrons are incorrect, leading to the lowest energy gap away from the K point and a lack of CB maximum at the Q point. Hence the simplest nearest-neighbor tunneling model which successfully describes Dirac fermions in graphene captures the opening of the gap at K point of the BZ and composition of VB and CB wave functions in terms of d -Mo and p -S₂ orbitals. However, it fails to capture important properties of CB and VB away from the K points. In order to capture the effective masses of CB and VB bands and CB maximum leading to band nesting

we need to include tunneling between second neighbor Mo atoms.

IV. FIRST AND SECOND NEIGHBOR TUNNELING HAMILTONIAN

We now consider tunneling from the Mo atom to its six nearest-neighbor $\bar{R}_{A1}-\bar{R}_{A6}$ Mo atoms as illustrated in Fig. 1, with the same for sulfur dimers. The second neighbor tunneling matrix elements are parametrized by tunneling amplitudes W_i with dependence on \vec{k} expressed by functions $g_i(\vec{k})$. Explicit forms of $g_i(\vec{k})$ and W_i are given in Appendix B. The explicit form of the Hamiltonian contains now dispersion of and coupling between d and p orbitals:

$$H(\vec{k}) = \begin{pmatrix} E_{m_d=-2} + W_{1g0}(\vec{k}) & W_3 g_2(\vec{k}) & W_4 g_4(\vec{k}) & V_1 f_{-1}(\vec{k}) & -V_2 f_0(\vec{k}) & V_3 f_1(\vec{k}) \\ & E_{m_d=0} + W_{2g0}(\vec{k}) & W_3 g_2(\vec{k}) & -V_4 f_0(\vec{k}) & -V_5 f_1(\vec{k}) & -V_4 f_{-1}(\vec{k}) \\ & & E_{m_d=2} + W_{1g0}(\vec{k}) & -V_3 f_1(\vec{k}) & -V_2 f_{-1}(\vec{k}) & V_1 f_0(\vec{k}) \\ E_{m_p=-1} + W_{5g0}(\vec{k}) & & & 0 & & W_7 g_2(\vec{k}) \\ & & & E_{m_p=0} + W_{6g0}(\vec{k}) & & 0 \\ & & & & & E_{m_p=1} + W_{5g0}(\vec{k}) \end{pmatrix}. \quad (9)$$

Figure 4 shows the energy bands obtained using first and second neighbor Hamiltonian, Eq. (9), black squares, and *ab initio* energy bands without spin-orbit (SO) coupling. By comparison with Fig. 3 we see that now the gap opens up across the entire BZ due to direct interaction of d orbitals on Mo atoms. The band structure in the vicinity of the K point is now significantly improved. The right hand side of the figure shows

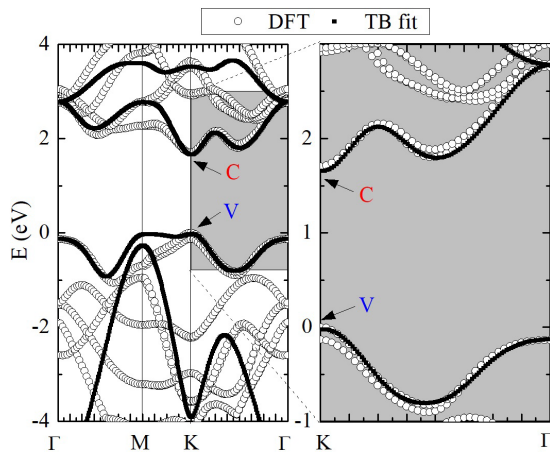


FIG. 4. First and second neighbor tunneling model. Black, nn tb model; white circles, DFT (no SO). Left: energy bands from K to Γ , K to M , and M to G points in the Brillouin zone obtained for Mo-S₂ first and second neighbor tunneling model. Note gap opened across entire BZ. Right: comparison of C and V bands close to K point. Note direct energy gap at K point, correct masses, and CB minimum at Q point.

excellent agreement of *ab initio* and TB, Eq. (9), conduction (CB), and valence (VB) energy bands. In particular, we see the emergence of the second minimum in the CB at Q point. The origin of the minimum at Q point is analyzed in the left panel of Fig. 5 where different colors mark contributions from

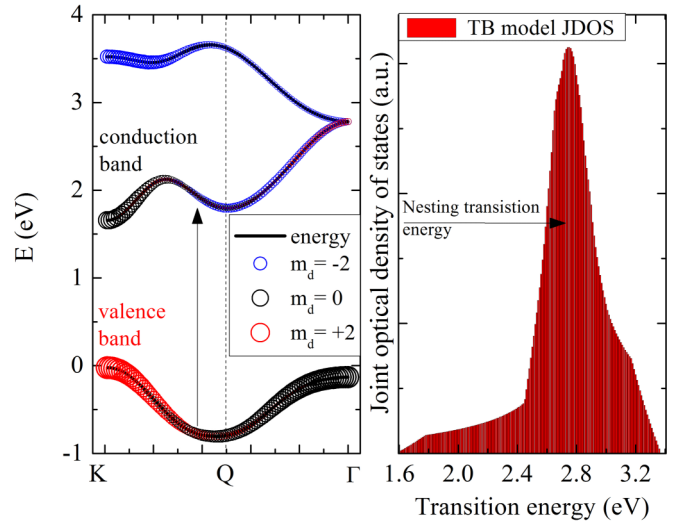


FIG. 5. Origin of Q point minima in CB and its effect on joint optical density of states. Left: evolution of energy bands from K to Q and from Q to Γ points in the Brillouin zone. In CB note $m_d = 0$ contribution at K and $m_d = -2$ at Q , while in VB note $m_d = +2$ at K and $m_d = 0$ at Q . Vertical arrows indicate VB to CB transitions. Right: joint optical density of states as a function of transition energy calculated for whole BZ.

different d orbitals. The size of circles denotes the contribution of different orbitals. At the K point the top of the VB is composed mainly of $m_d = 2$ orbital and the bottom of CB has $m_d = 0$ character. At the Γ point the top of the VB has $m_d = 0$ character and the bottom of the CB has $m_d = \pm 2$ character. Hence the higher energy band with $m_d = -2$ character has to cross the $m_d = 0$ CB. The crossing of $m_d = 0$ and $m_d = -2$ bands leads to a maximum in the conduction band followed by a second minimum at Q . Around the minimum at Q point the conduction and valence bands are parallel. This nesting of CB and VB leads to a maximum in joint optical density of states, shown in the right panel of Fig. 5 and discussed already by, e.g., Carvalho, Ribeiro, and Castro Neto [18].

We note that the minimal LCAO basis identified in this paper leads to excellent agreement of the *ab initio* and TB conduction and valence energy bands at the K point. However, we see that there exists a difference between *ab initio* and TB calculations in the vicinity of the M point—the CB and VB appear to be shifted up in energy. By comparison with Fig. 3 we see that in the absence of direct tunneling between metal d orbitals the two valence and conduction bands cross and the energy gap closes altogether in the vicinity of the M point. The tunneling between nearest-neighbor metal orbitals is solely responsible for the opening of the gap at the M points, while it only leads to modification of effective masses at the K points. Hence this region of the Brillouin zone is very sensitive to both tunneling between neighbors further apart and to inclusion of additional metal orbitals. As we are mainly interested in the K points and Q points of the BZ we leave the M points to future study.

V. EFFECTIVE TWO-BAND MASSIVE DIRAC FERMION MODEL

With the six-band model understood we now proceed to fit our results to the two-band massive Dirac fermion model applicable in the vicinity of K points. Following Kormányos *et al.* [44] we write our two-band Hamiltonian H_{2B} as a function of deviation q from the wave vector $k = K + q$ as

$$H_{2B}(\vec{k}) = a \cdot t \begin{pmatrix} \tau q_x - i q_y & \\ & \tau q_x + i q_y \end{pmatrix} + \frac{\Delta}{2} \begin{pmatrix} 1 & \\ & -1 \end{pmatrix} + \begin{pmatrix} \alpha q^2 & \\ & \beta q^2 \end{pmatrix} + \kappa \begin{pmatrix} & q_+^2 \\ q_-^2 & \end{pmatrix} - \tau \frac{\eta}{2} q^2 \begin{pmatrix} & q_+ \\ q_- & \end{pmatrix}, \quad (10)$$

where $q_{\pm} = q_x \pm q_y$ and $\tau = \pm 1$ for $K, -K$ valleys. Figure 6 shows the results of fitting eigenenergies of Eq. (10) to our *ab initio* results and results obtained by $k \cdot p$ theory of Kormányos *et al.* [44]. We see a good agreement of all three results. The two-band model parameters used in Fig. 6 are $a = 3.193 \text{ \AA}$, $t = 1.4111 \text{ eV}$, $\Delta = 1.6850 \text{ eV}$, $\alpha = 0.8341 \text{ eV \AA}^2$, $\beta = 0.8066 \text{ eV \AA}^2$, $\kappa = -0.0354 \text{ eV \AA}^2$, and $\eta = -0.0833 \text{ eV \AA}^3$. For $\alpha = \beta = \kappa = \eta = 0$ Eq. (10) reduces to a massive Dirac fermion model proposed by Xiao *et al.* [9] for the description of conduction and valence bands close to the K point. Note that wave vector k is measured from the K point. Best parameters

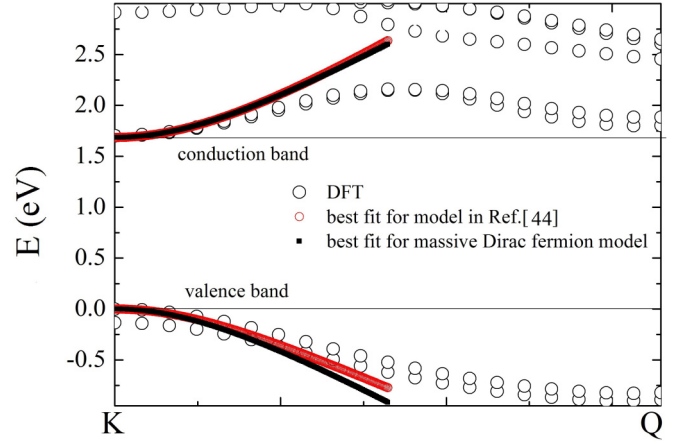


FIG. 6. Energy dispersion of effective massive Dirac fermion model in the vicinity of K point: DFT (empty circles); Ref. [44] (red circles); this work (black squares).

for the massive Dirac fermion model are $a = 1.46 \text{ \AA}$, $t = 1.4677 \text{ eV}$, and $\Delta = 1.6848 \text{ eV}$.

VI. MAGNETIC FIELD: LANDÉ g FACTORS

We now describe the response of TMDCs to the applied magnetic field [12,24,37,40,46,49–61]. The perpendicular magnetic field B couples to the orbital angular momentum L as $H_2 = \mu_B B_z L_z$. From symmetry analysis at the K point the wave functions of the conduction band are composed of $m_d = 0$ and $m_p = -1$ orbitals as

$$\begin{aligned} \Psi_{CB}^{\uparrow}(\vec{K}, \vec{r}) &= \frac{A_{m_d=0}^{\vec{K}=\vec{K}}(CB)}{\sqrt{N_{UC}}} \sum_{i=1}^{N_{UC}} e^{i\vec{K} \cdot \vec{R}_{A,i}} \phi_{l=2, m_d=0}(\vec{r} - \vec{R}_{A,i}) \\ &+ \frac{B_{m_p=-1}^{\vec{K}=\vec{K}}(CB)}{\sqrt{N_{UC}}} \sum_{i=1}^{N_{UC}} e^{i\vec{K} \cdot \vec{R}_{B,i}} \phi_{l=1, m_p=-1}(\vec{r} - \vec{R}_{B,i}). \end{aligned} \quad (11)$$

With details of the analysis found in Appendix C the energy of electron in CB at K point is given by the contributions from the $m_d = 0$ orbital, equal to zero, and finite contribution from $m_p = -1$ orbital as

$$\begin{aligned} E_{CB}(\vec{K}) &= \langle \Psi_{CB}^{\uparrow}(\vec{K}) | \hat{L}_z / \hbar | \Psi_{CB}^{\uparrow}(\vec{K}) \rangle \mu_B B_z \\ &= (-1) |B_{m_p=-1}^{\vec{K}=\vec{K}}(CB)|^2 \mu_B B_z. \end{aligned}$$

At $-K$ point the energy of electron in CB is given by the contributions from the $m_d = 0$ orbital (no contribution) and contribution from $m_p = +1$ orbital as

$$\begin{aligned} E_{CB}(-\vec{K}) &= \langle \Psi_{CB}^{\uparrow}(-\vec{K}) | \hat{L}_z / \hbar | \Psi_{CB}^{\uparrow}(-\vec{K}) \rangle \mu_B B_z \\ &= (+1) |B_{m_p=+1}^{\vec{K}=-\vec{K}}(CB)|^2 \mu_B B_z. \end{aligned}$$

The valley Landé energy splitting $\Delta_{\text{VL}}^{\text{CB}}$ in the conduction band is given by

$$\begin{aligned}\Delta_{\text{VL}}^{\text{CB}} &= E_{\text{CB}}(+\vec{K}) - E_{\text{CB}}(-\vec{K}) \\ &= [-1|B_{m_p=-1}^{\vec{k}=\vec{K}}(\text{CB})|^2 - 1|B_{m_p=+1}^{\vec{k}=-\vec{K}}(\text{CB})|^2]\mu_B B_z \\ &= (-2)|B_{m_p=-1}^{\vec{k}=\vec{K}}(\text{CB})|^2\mu_B B_z,\end{aligned}\quad (12)$$

where we used the fact that orbital compositions of $m_p = \pm 1$ orbitals at K and $-K$ are equal. A similar analysis carried out for the valley Landé energy splitting $\Delta_{\text{VL}}^{\text{VB}}$ in the valence band gives

$$\Delta_{\text{VL}}^{\text{VB}} = 2(2|A_{m_d=2}^{\vec{k}=\vec{K}}(\text{VB})|^2 + 1|B_{m_p=+1}^{\vec{k}=\vec{K}}(\text{VB})|^2)\mu_B B_z.$$

Using results from the six band model, Eq. (9), gives the effective Landé g factors of $g_{\text{VL}}^{\text{CB}} = -2|B_{m_p=-1}^{\vec{k}=\vec{K}}(\text{CB})|^2 = -0.4$ in the conduction band and $\Delta_{\text{VL}}^{\text{VB}} = 2(2|A_{m_d=2}^{\vec{k}=\vec{K}}(\text{VB})|^2 + 1|B_{m_p=+1}^{\vec{k}=\vec{K}}(\text{VB})|^2)\mu_B B_z = 3.996$.

By comparison, values deduced from Ref. [36] give $g_{\text{VL}}^{\text{CB}} = -0.88$, $g_{\text{VL}}^{\text{VB}} = 3.20$ and those from Ref. [34] give $g_{\text{VL}}^{\text{CB}} = -0.24$, $g_{\text{VL}}^{\text{VB}} = 3.44$.

VII. MAGNETIC FIELD: VALLEY ZEEMAN AND LANDAU g FACTORS

We now discuss valley Zeeman splitting due to Landau quantization. We start with the massive Dirac Hamiltonian for K point derived in Eq. (10):

$$H_{2B}(\vec{k}) = \frac{\Delta}{2} \begin{pmatrix} 1 & \\ & -1 \end{pmatrix} + v_F \begin{pmatrix} & \tau q_x - i q_y \\ \tau q_x + i q_y & \end{pmatrix}. \quad (13)$$

With magnetic field $\vec{B} = B\hat{z}$ in the symmetric gauge, vector potential $\vec{A} = B/2(-y, x, 0)$. We substitute $\vec{q} \rightarrow \vec{q} + e/c\vec{A}$ and measure length in units of magnetic length $r \rightarrow r/l_0$, where $l_0 = \sqrt{eB/c}$. Transformation into creation and annihilation operators [62]

$$\begin{aligned}\hat{a}^\dagger &= \frac{1}{\sqrt{2}} \left(-\partial_x - i\partial_y + \frac{1}{2}(x + iy) \right), \\ \hat{a} &= \frac{1}{\sqrt{2}} \left(\partial_x - i\partial_y + \frac{1}{2}(x - iy) \right)\end{aligned}\quad (14)$$

gives a massive Dirac fermion Hamiltonian in magnetic field as

$$H_{\text{mDF}}(\vec{k}) = \frac{\Delta}{2} \begin{pmatrix} 1 & \\ & -1 \end{pmatrix} + v \begin{pmatrix} & -i\hat{a} \\ i\hat{a}^\dagger & \end{pmatrix}, \quad (15)$$

where $v = \sqrt{2}v_F/l_0$. The eigenfunctions $\Psi_{n,m}^{C/V} = (\alpha_n^{C/V}|n-1, m\rangle, \beta_n^{C/V}|n, m\rangle)^T$ of the Hamiltonian, Eq. (15), are spinors in the basis of CB and VB states at K ($-K$), with eigenenergies of the n th Landau level $E_n^{C/V} = \pm\sqrt{(\Delta/2)^2 + v^2n}$. Here, massive Dirac fermion nature manifests itself in eigenvectors expressed as a combination of states with different n , which differs for both valleys. The energy spectrum contains three types of states for K and $-K$ points: positive (negative) energies with $n \geq 1$ for conduction (valence) band states indicated by indices $C(V)$ and $n = 0$ Landau level (OLL) in each valley. The key result [49,50] is that in the K valley the OLL is

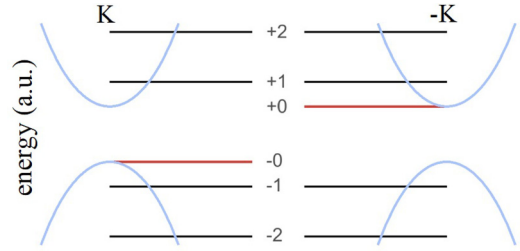


FIG. 7. Landau energy levels at K and $-K$ points. Note the splitting of the (0)-energy level—it is attached to the top of the valence band at K and to the bottom of the CB at $-K$ point. The energy difference of Landau $n = +1$ level at $+K$ and $n = 0$ Landau level at $-K$ gives valley Zeeman splitting.

attached to the top of the valence band (negative energy), while in the $-K$ valley OLL is attached to the bottom of the conduction band (positive energy). Figure 7 shows the energy spectrum for K and $-K$ valleys, with $n = 0$ LL shown in red.

The valley Zeeman splitting in the conduction band is given by the energy difference between an electron in $+K$ valley, $E_1(+K) = \sqrt{(\Delta/2)^2 + (\sqrt{2}v_F/l_0)^2}$, and an electron in the $-K$ valley $E_0(-K) = \sqrt{(\Delta/2)^2 + (\sqrt{2}v_F/l_0)^2}$:

$$\begin{aligned}\Delta_{\text{VZ}} &= E_1^C(K) - E_0^C(-K) = \frac{\Delta}{2} \left(\sqrt{1 + \left(\frac{2v}{\Delta l_0} \right)^2} - 1 \right) \\ &\approx \frac{\Delta}{2} \left(\frac{\sqrt{2}v_F}{\Delta l_0} \right)^2 = \Delta \left(\frac{v_F}{\Delta l_0} \right)^2 \hbar \omega_c,\end{aligned}\quad (16)$$

where $\hbar \omega_c$ is the cyclotron energy. We see that valley Zeeman splitting is proportional to the cyclotron energy and the ratio of Fermi velocity to the energy gap [61].

We can now compare the valley Landé and Zeeman contributions for MoS_2 . For magnetic field $B = 1$ T, we obtain the following values of splitting:

$$\Delta_{\text{VL}}^{\text{CB}} = -2|B_{m_p=-1}^{\text{CB}}(K)|^2\mu_B B = -0.023 \text{ meV}, \quad (17)$$

$$\Delta_{\text{VL}}^{\text{VB}} = 2(2|A_{m_d=2}^{\text{CB}}|^2 + 1|B_{m_p=-1}^{\text{CB}}|^2)\mu_B B = 0.231 \text{ meV}, \quad (18)$$

$$\Delta_{\text{VZ}} = \Delta \left(\frac{v_F}{\Delta} \right)^2 \hbar \omega_c = \Delta \left(\frac{v_F}{\Delta} \right)^2 \hbar \frac{eB}{m_0} = 1.395 \text{ meV}. \quad (19)$$

The first two values are in excellent agreement with recently reported [51] experimental Landé splitting of approximately $0.230 \text{ meV } T^{-1}$.

We now discuss the effect of spin-orbit interaction on the Landau level spectrum. The Hamiltonian for both spin down and up at the K point can be written as

$$H = \begin{pmatrix} \frac{\Delta}{2} - \frac{\Delta_{\text{SO}}}{2} & -iv\hat{a} \\ iv\hat{a}^\dagger & -\frac{\Delta}{2} - \frac{\Delta_{\text{SO}}}{2} \\ & & \frac{\Delta}{2} + \frac{\Delta_{\text{SO}}}{2} & -iv\hat{a} \\ & & iv\hat{a}^\dagger & -\frac{\Delta}{2} + \frac{\Delta_{\text{SO}}}{2} \end{pmatrix}, \quad (20)$$

where $\Delta_{\text{SO}}^{\text{C/V}}$ is the spin splitting for the conduction (valence) band. In analogy with Eq. (15) we obtain the eigenvectors $\Psi_{n,m}^{\pm,\sigma} = (\alpha_{n,\sigma}^{\text{C/V},\Delta_{\text{SO}}} |n-1,m\rangle, \beta_{n,\sigma}^{\text{C/V},\Delta_{\text{SO}}} |n,m\rangle)^T$ for K and eigenvectors $\Psi_{n,m}^{\pm,\sigma} = ((\alpha_{n,\sigma}^{\text{C/V},-\Delta_{\text{SO}}})^* |n,m\rangle, \beta_{n,\sigma}^{\text{C/V},-\Delta_{\text{SO}}} |n-1,m\rangle)^T$ for the $-K$ valley. The corresponding eigenvalues are given by $E_{n,\sigma}^{\text{C/V}} = \sigma(\Delta_{\text{SO}}^{\text{C}} + \Delta_{\text{SO}}^{\text{V}})/4 \pm \sqrt{(\Delta + \sigma(\Delta_{\text{SO}}^{\text{C}} - \Delta_{\text{SO}}^{\text{V}})/2)^2/4 + v^2 n}$, where $\sigma = \pm 1$ for spin up or down. The LL spectrum becomes even more asymmetric between the valleys. Because of the interaction between valence and conduction band the strong SO coupling in the valence band leads to spin splitting in the conduction band.

VIII. CONCLUSIONS

We presented here a tight-binding theory of transition metal dichalcogenides. We derived an effective tight-binding Hamiltonian and elucidated the electron tunneling from metal to dichalcogenides orbitals at different points of the BZ. This allowed us to discuss the band gaps at K points in the BZ, the origin of secondary conduction band minima at Q points, and their role in band nesting and strong light matter interaction. The Landé and Zeeman valley splitting as well as the effective mass Dirac fermion Hamiltonian in the magnetic field was determined.

ACKNOWLEDGMENTS

M.B. acknowledges financial support from National Science Center (NCN), Poland, Grant Sonata No. 2013/11/D/ST3/02703. L.S. and P.H. acknowledge support from NSERC and uOttawa University Research Chair in Quantum Theory of Materials, Nanostructures and Devices. One of us (P.H.) thanks J. Kono, S. Crooker, A. Stier, and M. Potemski for discussions.

APPENDIX A: NEAREST-NEIGHBOR MATRIX ELEMENTS

Matrix elements of the nearest-neighbor tunneling Hamiltonian, Eq. (8), are expressed by k -independent parameters V_i

$$\begin{aligned} V_1 &= \frac{1}{\sqrt{2}} \left[\frac{\sqrt{3}}{2} \left(\frac{d_{\perp}^2}{d^2} - 1 \right) V_{dp\sigma} - \left(\frac{d_{\perp}^2}{d^2} + 1 \right) V_{dp\pi} \right] \frac{d_{\parallel}}{d}, \\ V_2 &= \frac{1}{2} [\sqrt{3} V_{dp\sigma} - 2 V_{dp\pi}] \frac{d_{\perp}}{d} \left(\frac{d_{\parallel}}{d} \right)^2, \\ V_3 &= \frac{1}{\sqrt{2}} \left[\frac{\sqrt{3}}{2} V_{dp\sigma} - V_{dp\pi} \right] \left(\frac{d_{\parallel}}{d} \right)^3, \\ V_3 &= \frac{1}{\sqrt{2}} \left[\frac{\sqrt{3}}{2} V_{dp\sigma} - V_{dp\pi} \right] \left(\frac{d_{\parallel}}{d} \right)^3, \\ V_4 &= \frac{1}{2} \left[\left(3 \frac{d_{\perp}^2}{d^2} - 1 \right) V_{dp\sigma} - 2\sqrt{3} \frac{d_{\perp}^2}{d^2} V_{dp\pi} \right] \frac{d_{\parallel}}{d}, \\ V_5 &= \frac{1}{2} \left[\left(3 \frac{d_{\perp}^2}{d^2} - 1 \right) V_{dp\sigma} - 2\sqrt{3} \left(\frac{d_{\perp}^2}{d^2} - 1 \right) V_{dp\pi} \right] \frac{d_{\perp}}{d} \end{aligned} \quad (\text{A1})$$

TABLE I. Slater-Koster parameters fitted to DFT band structure.

Parameter	Best fit (in eV)	Parameter	Best fit (in eV)
$E_{m_d=0,\pm 2}$	-0.03	$V_{dd\sigma}$	-1.10
$E_{m_p=\pm 1}$	-3.36	$V_{dd\pi}$	0.76
$E_{m_p=0}$	-4.78	$V_{dd\delta}$	0.27
$V_{dp\sigma}$	-3.39	$V_{pp\sigma}$	1.19
$V_{dp\pi}$	1.10	$V_{pp\pi}$	-0.83

and k -dependent factors ($k_x d_{\parallel} \rightarrow k_x, k_y d_{\parallel} \rightarrow k_y$)

$$\begin{aligned} f_0(\vec{k}) &= e^{ik_x} + e^{-ik_x/2} e^{i\sqrt{3}k_y/2} e^{-i2\pi/3} \\ &\quad + e^{-ik_x/2} e^{-i\sqrt{3}k_y/2} e^{i2\pi/3}, \\ f_{-1}(\vec{k}) &= e^{ik_x} + e^{-ik_x/2} e^{i\sqrt{3}k_y/2} e^{i2\pi/3} \\ &\quad + e^{-ik_x/2} e^{-i\sqrt{3}k_y/2} e^{-i2\pi/3}, \\ f_{+1}(\vec{k}) &= e^{ik_x} + e^{-ik_x/2} e^{i\sqrt{3}k_y/2} + e^{-ik_x/2} e^{-i\sqrt{3}k_y/2}. \end{aligned} \quad (\text{A2})$$

APPENDIX B: NEXT-NEAREST-NEIGHBOR MATRIX ELEMENTS

Parameters of the second neighbor tunneling in Eq. (9) are given by k -independent terms W_i

$$\begin{aligned} W_1 &= \frac{1}{8} (3V_{dd\sigma} + 4V_{dd\pi} + V_{dd\delta}), \\ W_2 &= \frac{1}{4} (V_{dd\sigma} + 3V_{dd\delta}), \\ W_3 &= -\frac{\sqrt{3}}{4\sqrt{2}} (V_{dd\sigma} - V_{dd\delta}), \\ W_4 &= \frac{1}{8} (3V_{dd\sigma} - 4V_{dd\pi} + V_{dd\delta}), \\ W_5 &= \frac{1}{2} (V_{pp\sigma} + V_{pp\pi}), \\ W_6 &= V_{pp\pi}, \\ W_7 &= \frac{1}{2} (V_{pp\sigma} - V_{pp\pi}), \end{aligned} \quad (\text{B1})$$

and k -dependent functions g_i

$$\begin{aligned} g_0(\vec{k}) &= 4 \cos(3k_x/2) \cos(\sqrt{3}k_y/2) + 2 \cos(\sqrt{3}k_y), \\ g_2(\vec{k}) &= -2 \cos(\sqrt{3}k_y) + 2 \cos(3k_x/2 + \sqrt{3}k_y/2) e^{i\pi/3} \\ &\quad + 2 \cos(3k_x/2 - \sqrt{3}k_y/2) e^{-i\pi/3}, \\ g_4(\vec{k}) &= 2 \cos(\sqrt{3}k_y) + 2 \cos(3k_x/2 + \sqrt{3}k_y/2) e^{i2\pi/3} \\ &\quad + 2 \cos(3k_x/2 - \sqrt{3}k_y/2) e^{-i2\pi/3}. \end{aligned} \quad (\text{B2})$$

Slater-Koster parameters found by fitting our second nearest-neighbor model to DFT band structure used to create Fig. 4 and Fig. 5 are given in Table I.

APPENDIX C: LANDÉ g FACTOR

To calculate the Landé g factor in perpendicular magnetic field B_z we first analyze the expectation value of L_z operator

for wave functions of A and B sublattices written as

$$\Psi_A^m(\vec{k}, \vec{r}) = \frac{1}{\sqrt{N_{UC}}} \sum_{i=1}^{N_{UC}} e^{i\vec{k} \cdot \vec{R}_{A,i}} \varphi_m(\vec{r} - \vec{R}_{A,i}),$$

$$\Psi_B^l(\vec{k}, \vec{r}) = \frac{1}{\sqrt{N_{UC}}} \sum_{j=1}^{N_{UC}} e^{i\vec{k} \cdot \vec{R}_{B,j}} \varphi_l(\vec{r} - \vec{R}_{B,j}). \quad (\text{C1})$$

For $L_z = -i\hbar(\vec{r} \times \vec{\nabla}_{\vec{r}})_z$ we have therefore

$$\begin{aligned} & \langle \Psi_B^l(\vec{k}, \vec{r}) | (-i\hbar)(\vec{r} \times \vec{\nabla}_{\vec{r}})_z | \Psi_A^m(\vec{k}, \vec{r}) \rangle \\ &= \frac{-i\hbar}{N_{UC}} \sum_{i,j=1}^{N_{UC}} \int d\vec{r} e^{i\vec{k} \cdot \vec{R}_{AB}} \varphi_l^*(\vec{r} - \vec{R}_{B,j}) (\vec{r} \times \vec{\nabla}_{\vec{r}})_z \varphi_m(\vec{r} - \vec{R}_{A,i}), \end{aligned} \quad (\text{C2})$$

where $\vec{R}_{AB} = \vec{R}_{A,i} - \vec{R}_{B,j}$. To evaluate Eq. (C2) we introduce new variables $\vec{u}_i = \vec{r} - \vec{R}_{A,i}$ to analyze the action of operator $\vec{\nabla}_{\vec{r}}$ on orbitals localized at $\vec{R}_{A,i}$:

$$\left(\vec{r} \times \frac{\partial}{\partial \vec{r}} \right) \varphi_m(\vec{r} - \vec{R}_{A,i}) = m \varphi_m(\vec{u}_i) + (\vec{R}_{A,i} \times \vec{p}_{u_i})_z \varphi_m(\vec{u}_i). \quad (\text{C3})$$

Using this and shifting variables on sites B as $\vec{r} - \vec{R}_{B,j} = \vec{u}_i + \vec{R}_{A,i} - \vec{R}_{B,j}$, we obtain

$$\begin{aligned} & \langle \Psi_B^l(\vec{k}, \vec{r}) | (-i\hbar)(\vec{r} \times \vec{\nabla}_{\vec{r}})_z | \Psi_A^m(\vec{k}, \vec{r}) \rangle \\ &= m \frac{(-i\hbar)}{N_{UC}} \sum_{\vec{R}_{AB}, \vec{R}_A}^{N_{UC}} \int d\vec{u} e^{i\vec{k} \cdot \vec{R}_{AB}} \underbrace{\varphi_l^*(\vec{u} + \vec{R}_{AB}) \varphi_m(\vec{u})}_{\neq 0 \text{ only for } \vec{R}_{AB}=0} \end{aligned}$$

$$\begin{aligned} & + \frac{(-i\hbar)}{N_{UC}} \sum_{\vec{R}_{AB}, \vec{R}_A}^{N_{UC}} \int d\vec{u} e^{i\vec{k} \cdot \vec{R}_{AB}} \varphi_l^*(\vec{u} + \vec{R}_{AB}) \\ & \times (\vec{R}_A \times \vec{p}_{\vec{u}_i})_z \varphi_m(\vec{u}). \end{aligned} \quad (\text{C4})$$

The first term on the right hand side of Eq. (C4) can be more transparently written as

$$\begin{aligned} & m \frac{(-i\hbar)}{N_{UC}} \sum_{\vec{R}_A}^{N_{UC}} \underbrace{\int d\vec{u} \varphi_l^*(\vec{u}) \varphi_m(\vec{u})}_{\delta_{lm}} \\ &= m \frac{(-i\hbar)}{N_{UC}} \sum_{\vec{R}_A}^{N_{UC}} \delta_{lm} = m \frac{(-i\hbar)}{N_{UC}} N_{UC} \delta_{lm} = (-i\hbar) m \delta_{lm}, \end{aligned} \quad (\text{C5})$$

while the second term vanishes,

$$\begin{aligned} & \frac{(-i\hbar)}{N_{UC}} \sum_{\vec{R}_A}^{N_{UC}} \left[\underbrace{\sum_{\vec{R}_{AB}}^{N_{UC}} e^{i\vec{k} \cdot \vec{R}_{AB}} \int d\vec{u} \varphi_l^*(\vec{u} + \vec{R}_{AB}) (\vec{p}_{\vec{u}_i})_z \varphi_m(\vec{u})}_{\vec{R}_A \text{ independent}} \right] \\ &= 0, \end{aligned} \quad (\text{C6})$$

because the sum over \vec{R}_A is taken over an isotropic system. Finally, we get

$$\langle \Psi_B^l(\vec{k}, \vec{r}) | (-i\hbar)(\vec{r} \times \vec{\nabla}_{\vec{r}})_z | \Psi_A^m(\vec{k}, \vec{r}) \rangle = (-i\hbar) m \delta_{lm}, \quad (\text{C7})$$

which is used to calculate Landé energy splitting, e.g., for conduction band $E_{CB}(\pm K) = (\mp 1) |B_{m_p=\mp 1}^{K=K}(CB)|^2 \mu_B B_z$. Analogous analysis can be performed for the valence band.

-
- [1] G. Connell, J. Wilson, and A. Yoffe, *J. Phys. Chem. Solids* **30**, 287 (1969).
- [2] M. V. Bollinger, J. V. Lauritsen, K. W. Jacobsen, J. K. Nørskov, S. Helveg, and F. Besenbacher, *Phys. Rev. Lett.* **87**, 196803 (2001).
- [3] K. F. Mak, C. Lee, J. Hone, J. Shan, and T. F. Heinz, *Phys. Rev. Lett.* **105**, 136805 (2010).
- [4] A. Splendiani, L. Sun, Y. Zhang, T. Li, J. Kim, C.-Y. Chim, G. Galli, and F. Wang, *Nano Lett.* **10**, 1271 (2010).
- [5] B. Radisavljevic, A. Radenovic, J. Brivio, V. Giacometti, and A. Kis, *Nat. Nanotechnol.* **6**, 147 (2011).
- [6] A. Kuc, N. Zibouche, and T. Heine, *Phys. Rev. B* **83**, 245213 (2011).
- [7] E. S. Kadantsev and P. Hawrylak, *Solid State Commun.* **152**, 909 (2012).
- [8] T. Cheiwchanchamnangij and W. R. L. Lambrecht, *Phys. Rev. B* **85**, 205302 (2012).
- [9] D. Xiao, G.-B. Liu, W. Feng, X. Xu, and W. Yao, *Phys. Rev. Lett.* **108**, 196802 (2012).
- [10] K. F. Mak, K. He, J. Shan, and T. F. Heinz, *Nat. Nanotechnol.* **7**, 494 (2012).
- [11] T. Cao, G. Wang, W. Han, H. Ye, C. Zhu, J. Shi, Q. Niu, P. Tan, E. Wang, B. Liu, and J. Feng, *Nat. Commun.* **3**, 887 (2012).
- [12] G. Sallen, L. Bouet, X. Marie, G. Wang, C. R. Zhu, W. P. Han, Y. Lu, P. H. Tan, T. Amand, B. L. Liu, and B. Urbaszek, *Phys. Rev. B* **86**, 081301(R) (2012).
- [13] G. Kioseoglou, A. T. Hanbicki, M. Currie, A. L. Friedman, D. Gunlycke, and B. T. Jonker, *Appl. Phys. Lett.* **101**, 221907 (2012).
- [14] Q. H. Wang, K. Kalantar-Zadeh, A. Kis, J. N. Coleman, and M. S. Strano, *Nat. Nanotechnol.* **7**, 699 (2012).
- [15] A. M. Jones, H. Yu, N. J. Ghimire, S. Wu, G. Aivazian, J. S. Ross, B. Zhao, J. Yan, D. G. Mandrus, D. Xiao, W. Yao, and X. Xu, *Nat. Nanotechnol.* **8**, 634 (2013).
- [16] J. S. Ross, S. Wu, H. Yu, N. J. Ghimire, A. M. Jones, G. Aivazian, J. Yan, D. G. Mandrus, D. Xiao, W. Yao, and X. Xu, *Nat. Commun.* **4**, 1474 (2013).
- [17] A. A. Mitoglu, P. Plochocka, J. N. Jadczyk, W. Escoffier, G. L. J. A. Rikken, L. Kulyuk, and D. K. Maude, *Phys. Rev. B* **88**, 245403 (2013).
- [18] A. Carvalho, R. M. Ribeiro, and A. H. Castro Neto, *Phys. Rev. B* **88**, 115205 (2013).

- [19] A. K. Geim and I. V. Grigorieva, *Nature (London)* **499**, 419 (2013).
- [20] X. Xu, W. Yao, D. Xiao, and T. F. Heinz, *Nat. Phys.* **10**, 343 (2014).
- [21] Y. Zhang, T.-R. Chang, B. Zhou, Y.-T. Cui, H. Yan, Z. Liu, F. Schmitt, J. Lee, R. Moore, Y. Chen *et al.*, *Nat. Nanotechnol.* **9**, 111 (2014).
- [22] Z. Ye, T. Cao, K. O'Brien, H. Zhu, X. Yin, Y. Wang, S. G. Louie, and X. Zhang, *Nature (London)* **513**, 214 (2014).
- [23] Y. Zhang, T. Oka, R. Suzuki, J. Ye, and Y. Iwasa, *Science* **344**, 725 (2014).
- [24] T. Scrase, Y. Tsai, B. Barman, L. Schweidenback, A. Petrou, G. Kioseoglou, I. Ozfidan, M. Korkusiński, and P. Hawrylak, *Nat. Nanotechnol.* **10**, 603 (2015).
- [25] F. Withers, O. Del Pozo-Zamudio, S. Schwarz, S. Dufferwiel, P. M. Walker, T. Godde, A. P. Rooney, A. Gholinia, C. R. Woods, P. Blake *et al.*, *Nano Lett.* **15**, 8223 (2015).
- [26] K. He, N. Kumar, L. Zhao, Z. Wang, K. F. Mak, H. Zhao, and J. Shan, *Phys. Rev. Lett.* **113**, 026803 (2014).
- [27] G. Wang, E. Palneau, T. Amand, S. Tongay, X. Marie, and B. Urbaszek, *Appl. Phys. Lett.* **106**, 112101 (2015).
- [28] X.-X. Zhang, Y. You, S. Y. F. Zhao, and T. F. Heinz, *Phys. Rev. Lett.* **115**, 257403 (2015).
- [29] A. Arora, K. Nogajewski, M. Molas, M. Koperski, and M. Potemski, *Nanoscale* **7**, 20769 (2015).
- [30] A. M. Jones, H. Yu, J. R. Schaibley, J. Yan, D. G. Mandrus, T. Taniguchi, K. Watanabe, H. Dery, W. Yao, and X. Xu, *Nat. Phys.* **12**, 323 (2016).
- [31] J. Jadcak, A. Delgado, L. Bryja, Y. S. Huang, and P. Hawrylak, *Phys. Rev. B* **95**, 195427 (2017).
- [32] H. Rostami, A. G. Moghaddam, and R. Asgari, *Phys. Rev. B* **88**, 085440 (2013).
- [33] G.-B. Liu, W.-Y. Shan, Y. Yao, W. Yao, and D. Xiao, *Phys. Rev. B* **88**, 085433 (2013).
- [34] E. Cappelluti, R. Roldan, J. A. Silva-Guillen, P. Ordejon, and F. Guinea, *Phys. Rev. B* **88**, 075409 (2013).
- [35] F. Zahid, L. Liu, Y. Zhu, J. Wang, and H. Guo, *AIP Adv.* **3**, 052111 (2013).
- [36] S. Fang, R. Kuate Defo, S. N. Shirodkar, S. Lieu, G. A. Tritsarlis, and E. Kaxiras, *Phys. Rev. B* **92**, 205108 (2015).
- [37] Y.-H. Ho, Y.-H. Wang, and H.-Y. Chen, *Phys. Rev. B* **89**, 155316 (2014).
- [38] G.-B. Liu, D. Xiao, Y. Yao, X. Xu, and W. Yao, *Chem. Soc. Rev.* **44**, 2643 (2015).
- [39] E. Ridolfi, D. Le, T. S. Rahman, E. R. Mucciolo, and C. H. Lewenkopf, *J. Phys.: Condens. Matter* **27**, 365501 (2015).
- [40] K. V. Shanavas and S. Satpathy, *Phys. Rev. B* **91**, 235145 (2015).
- [41] J. A. Silva-Guillen, P. San-Jose, and R. Roldan, *Appl. Sci.* **6**, 284 (2016).
- [42] A. J. Pearce, E. Mariani, and G. Burkard, *Phys. Rev. B* **94**, 155416 (2016).
- [43] F. Wu, F. Qu, and A. H. MacDonald, *Phys. Rev. B* **91**, 075310 (2015).
- [44] A. Kormányos, G. Burkard, M. Gmitra, J. Fabian, V. Zolyomi, N. D. Drummond, and V. Fal'ko, *2D Mater.* **2**, 022001 (2015).
- [45] A. Kormányos, P. Rakytá, and G. Burkard, *New J. Phys.* **17**, 103006 (2015).
- [46] G. Wang, L. Bouet, M. Glazov, T. Amand, E. Ivachenko, E. Palneau, X. Marie, and B. Urbaszek, *2D Mater.* **2**, 034002 (2015).
- [47] D. V. Rybkovskiy, I. C. Gerber, and M. V. Durnev, *Phys. Rev. B* **95**, 155406 (2017).
- [48] P. R. Wallace, *Phys. Rev.* **71**, 622 (1947).
- [49] M. O. Goerbig, R. Moessner, and B. Douçot, *Phys. Rev. B* **74**, 161407(R) (2006).
- [50] D. Xiao, W. Yao, and Q. Niu, *Phys. Rev. Lett.* **99**, 236809 (2007).
- [51] A. V. Stier, K. M. McCreary, B. T. Jonker, J. Kono, and S. A. Crooker, *Nat. Commun.* **7**, 10643 (2016).
- [52] D. MacNeill, C. Heikes, K. F. Mak, Z. Anderson, A. Kormányos, V. Zolyomi, J. Park, and D. C. Ralph, *Phys. Rev. Lett.* **114**, 037401 (2015).
- [53] Y. Li, J. Ludwig, T. Low, A. Chernikov, X. Cui, G. Arefe, Y. D. Kim, A. M. van der Zande, A. Rigosi, H. M. Hill *et al.*, *Phys. Rev. Lett.* **113**, 266804 (2014).
- [54] G. Aivazian, Z. Gong, A. M. Jones, R.-L. Chu, J. Yan, D. G. Mandrus, C. Zhang, D. Cobden, W. Yao, and X. Xu, *Nat. Phys.* **11**, 148 (2015).
- [55] A. Srivastava, M. Sidler, A. V. Allain, D. S. Lembke, A. Kis, and A. Imamoglu, *Nat. Phys.* **11**, 141 (2015).
- [56] H. Zeng, J. Dai, W. Yao, D. Xiao, and X. Cui, *Nat. Nanotechnol.* **7**, 490 (2012).
- [57] G. Plechinger, P. Nagler, A. Arora, A. Granados del Aguila, M. V. Ballottin, T. Frank, P. Steinleitner, M. Gmitra, J. Fabian, P. C. M. Christianen *et al.*, *Nano Lett.* **16**, 7899 (2016).
- [58] A. A. Mitioglu, K. Galkowski, A. Surrente, L. Klopotoski, D. Dumcenco, A. Kis, D. K. Maude, and P. Plochocka, *Phys. Rev. B* **93**, 165412 (2016).
- [59] Z. Wang, J. Shan, and K. F. Mak, *Nat. Nanotechnol.* **12**, 144 (2017).
- [60] G. Wang, X. Marie, B. L. Liu, T. Amand, C. Robert, F. Cadiz, P. Renucci, and B. Urbaszek, *Phys. Rev. Lett.* **117**, 187401 (2016).
- [61] T. Cai, S. A. Yang, X. Li, F. Zhang, J. Shi, W. Yao, and Q. Niu, *Phys. Rev. B* **88**, 115140 (2013).
- [62] P. Hawrylak, *Phys. Rev. Lett.* **71**, 3347 (1993).